








Collinear three-photon excitation of a strongly forbidden optical clock transition

Samuel P. Carman ^{1,*}, Jan Rudolph ^{1,2,*}, Benjamin E. Garber ^{1,*}, Michael J. Van de Graaff ¹, Hunter Swan ¹,
Yijun Jiang (姜一君) ³, Megan Nantel ³, Mahiro Abe ¹, Rachel L. Barcklay ⁴, and Jason M. Hogan ^{1,†}

¹*Department of Physics, Stanford University, Stanford, California 94305, USA*

²*Fermi National Accelerator Laboratory, Batavia, Illinois 60510, USA*

³*Department of Applied Physics, Stanford University, Stanford, California 94305, USA*

⁴*Department of Electrical Engineering, Stanford University, Stanford, California 94305, USA*

(Dated: July 1, 2024)

The $^1S_0 - ^3P_0$ clock transition in strontium serves as the foundation for the world’s best atomic clocks and for gravitational wave detector concepts in clock atom interferometry. This transition is weakly allowed in the fermionic isotope ^{87}Sr but strongly forbidden in bosonic isotopes. Here we demonstrate coherent excitation of the clock transition in bosonic ^{88}Sr using a novel collinear three-photon process in a weak magnetic field. We observe Rabi oscillations with frequencies of up to 50 kHz using W/cm^2 laser intensities and Gauss-level magnetic field amplitudes. The absence of nuclear spin in bosonic isotopes offers decreased sensitivity to magnetic fields and optical lattice light shifts, enabling atomic clocks with reduced systematic errors. The collinear propagation of the laser fields permits the interrogation of spatially separated atomic ensembles with common laser pulses, a key requirement for dark matter searches and gravitational wave detection with next-generation quantum sensors.

Narrow optical transitions to long-lived atomic states are essential for many applications in metrology [1–3], precision timekeeping [4–6], and tests of fundamental physics [7–10]. The most accurate optical atomic clocks use $^1S_0 - ^3P_0$ singlet-to-triplet transitions in neutral atoms and ions (e.g. Sr, Yb, Mg, Al^+) [11–14]. These ultranarrow transitions are weakly allowed in fermions because of the hyperfine interaction, but are strongly forbidden in bosons, where a large external magnetic field is required to induce coupling [15–17]. Bosonic isotopes promise considerable advantages, such as their lack of nuclear spin, higher natural abundance, simplified laser cooling and state preparation, as well as the scalar polarizability of their clock states [5, 18]. To access these desirable properties, coherent multi-photon processes in bosons have been proposed [18–21]. Of particular interest is the three-photon excitation $^1S_0 \rightarrow ^3P_1 \rightarrow ^3S_1 \rightarrow ^3P_0$ [19, 22], using a set of laser frequencies readily available for laser cooling, repumping, and imaging.

Ostensibly, this coherent three-photon excitation cannot be driven with collinear laser beams due to angular momentum selection rules [23]. Instead, at least one of the beams must be sent from a different direction. This is easily accommodated in most clock applications, where the beams can even be arranged to eliminate the net momentum transfer to the atoms [22, 24]. In contrast, collinear laser beams are advantageous in applications where several atomic ensembles are ideally addressed with identical laser pulses, such as multi-qubit entanglement in optical tweezer arrays [25–28], differential operation of atomic clocks [29–34], and gradiometer configurations in clock atom interferometry [35, 36]. In gradiometers, common laser pulses are particularly important for laser frequency noise suppression, which requires that all spectral content must be delivered from the same direction [37]. Like clocks, clock

atom interferometry proposals generally rely on naturally occurring narrow-line transitions in fermions [36]. Due to the weak coupling, interferometry pulses on these transitions are slow and the interferometer sensitivity is ultimately limited by the number of pulses that can be applied. Unlocking bosonic isotopes for long-baseline clock atom interferometry via multi-photon processes could lead to a substantial increase in sensitivity by engineering an effective transition with both strong coupling and long excited state lifetime.

Here we demonstrate a coherent, collinear three-photon process $^1S_0 \rightarrow ^3P_1 \rightarrow ^3S_1 \rightarrow ^3P_0$ in bosonic ^{88}Sr mediated by a weak magnetic bias field. The constant field lifts the degeneracy of the intermediate 3P_1 sublevels that otherwise leads to destructive interference of the excitation paths. We show why this transition cannot be driven with collinear laser beams without a magnetic field and illustrate the transformation of the effective angular wavefunction of 3P_1 under the associated external torque. We drive this three-photon transition using a single trichromatic laser pulse, delivered via a polarization-maintaining optical fiber. We observe Rabi oscillations between the clock states 1S_0 and 3P_0 with frequencies of up to 50 kHz, substantially surpassing what could be achieved with similar laser intensities on the naturally occurring single-photon transition in fermionic ^{87}Sr and the magnetic-field-induced transition in ^{88}Sr .

With this new technique, we demonstrate the first multi-photon clock atom interferometer using a Mach-Zehnder pulse sequence. Since all spectral content for the three-photon transition is copropagating, this interferometer scheme is compatible with long-baseline clock gradiometers like MAGIS-100 [36]. Bosonic isotopes can now be employed in such experiments, which extends the utility of next-generation quantum sensors.

Alkaline-earth-like atoms such as strontium have two valence electrons and their atomic states are split into a singlet and a triplet manifold [see Fig. 1(a)]. While strong electric dipole transitions are possible within each manifold, spin-flipping electric dipole transitions between singlet and triplet states are generally forbidden. A notable exception is the

* These authors contributed equally to this work.

† hogan@stanford.edu

$^1S_0 - ^3P_1$ transition, which is weakly allowed through spin-orbit coupling. The three-photon process described here combines this weak intercombination line and two strong electric dipole transitions into one coherent excitation.

The coupling strength of this multi-photon transition can be expressed as the product of the individual single-photon couplings Ω_i divided by the intermediate laser frequency detunings Δ_i [Fig. 1(b)]. When using linearly polarized light fields, the effective three-photon coupling can be written as

$$\Omega_{\text{eff}} = \frac{\Omega_1 \Omega_2 \Omega_3}{2\Delta_2} \epsilon_{jkl} D_{jn} e_n^{(1)} e_k^{(2)} e_l^{(3)}, \quad (1)$$

where ϵ_{jkl} is the Levi-Civita symbol, and $e_n^{(i)}$ is the n^{th} Cartesian component of the i^{th} laser's polarization vector, with an implicit sum over repeated indices (see Supplemental). The entries of the matrix D_{jn} depend on the inverse detunings $1/\Delta_{1,m}$ to the three magnetic sublevels m of 3P_1 . When these sublevels are degenerate, $D_{jn} = \frac{1}{\Delta_1} \delta_{jn}$ is diagonal and Eq. (1) reduces to

$$\Omega_{\text{eff}} = \frac{\Omega_1 \Omega_2 \Omega_3}{2\Delta_1 \Delta_2} \mathbf{e}^{(1)} \cdot (\mathbf{e}^{(2)} \times \mathbf{e}^{(3)}). \quad (2)$$

The three-photon coupling therefore scales with the volume spanned by the electric field polarization vectors, which vanishes for collinearly propagating optical fields.

Applying an external magnetic field \mathbf{B} along $\hat{\mathbf{z}}$ lifts the degeneracy of the 3P_1 sublevels via a Zeeman shift $\delta\omega_B = g_J \mu_B B/\hbar$, where g_J is the Landé g factor and μ_B is the Bohr magneton [see Fig. 1(b)]. Choosing a set of polarizations $\mathbf{e}^{(1)} = \mathbf{e}^{(2)} = \hat{\mathbf{x}}$ and $\mathbf{e}^{(3)} = \hat{\mathbf{z}}$ with collinear propagation direction $\hat{\mathbf{y}}$, the coupling becomes

$$\Omega_{\text{eff}} = \frac{\Omega_1 \Omega_2 \Omega_3}{4\Delta_2} \left(\frac{1}{\Delta_1 - \delta\omega_B} - \frac{1}{\Delta_1 + \delta\omega_B} \right). \quad (3)$$

The minus sign between the terms conveys the destructive interference of the two excitation paths (via $m = -1$ and $m = +1$) in the absence of a magnetic field.

The optical field requirements without external magnetic field can be illustrated using the angular part of the atomic wavefunction, which consists of an entangled superposition of orbital angular momentum \mathbf{L} and spin angular momentum \mathbf{S} [see Fig. 2(a)]. The light field at 689 nm along $\hat{\mathbf{x}}$ drives a weakly allowed singlet-to-triplet transition to 3P_1 only possible through spin-orbit coupling. The triplet component of the resulting state has the form $(|L_y\rangle|S_z\rangle - |L_z\rangle|S_y\rangle)$, where $|L_n\rangle$ and $|S_n\rangle$ are the Cartesian basis states of the orbital angular momentum and spin operators (see Supplemental). The axes of these p orbitals $|L_n\rangle$ are orthogonal to the polarization of the exciting laser. The other two light fields at 688 nm and 679 nm drive spin-preserving, dipole-allowed transitions where the polarization of the light has to match the p orbital axis of the associated spin projection $|S_n\rangle$. Since the final state of the three-photon process 3P_0 has the form $(|L_x\rangle|S_x\rangle + |L_y\rangle|S_y\rangle + |L_z\rangle|S_z\rangle)$, two mutually orthogonal polarization components are required to reach the appropriate spin state. Thus, Fig. 2(a) is a visual representation of

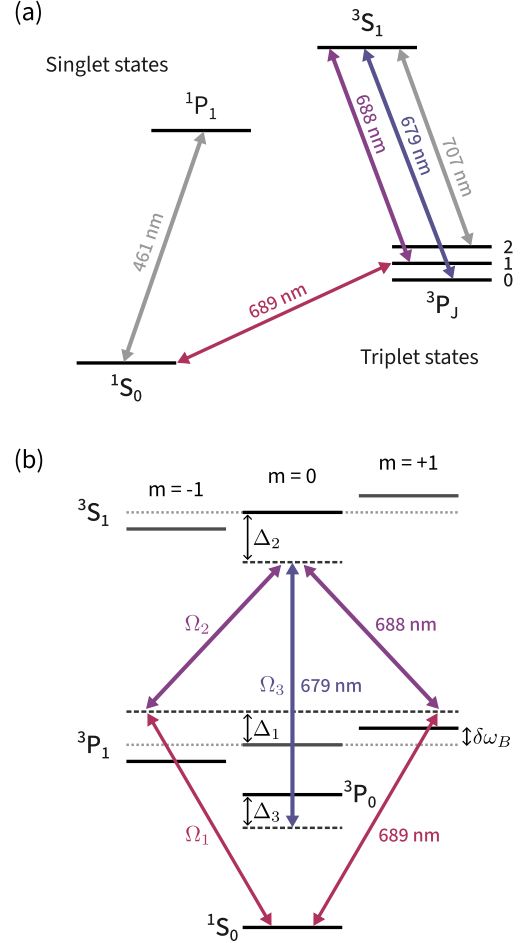


FIG. 1. (a) Singlet and triplet states of ^{88}Sr and the relevant transition wavelength connecting the atomic states. We describe a three-photon transition between 1S_0 and 3P_0 using laser light at 689 nm (magenta), 688 nm (purple), and 679 nm (blue). (b) Energy levels involved in the three-photon transition with Zeeman sublevels m in the presence of a magnetic field, causing a relative shift $\delta\omega_B$. The polarizations of the optical fields are linear, with 689 nm (Ω_1) and 688 nm (Ω_2) normal, and 679 nm (Ω_3) parallel to the quantization axis. Cumulative frequency detunings of the lasers from the respective $m = 0$ states are denoted by Δ_1 , Δ_2 , and Δ_3 .

the scalar triple product in Eq. (2), illustrating the need for non-copropagating light fields [38].

Applying a magnetic field along $\hat{\mathbf{z}}$ alters the angular part of the effective 3P_1 wavefunction

$$|^3P_1, \theta_B\rangle = -\frac{1}{\sqrt{2}} \left(\sin \theta_B |L_x\rangle + i \cos \theta_B |L_y\rangle \right) |S_z\rangle + \frac{1}{\sqrt{2}} |L_z\rangle \left(\sin \theta_B |S_x\rangle + i \cos \theta_B |S_y\rangle \right), \quad (4)$$

where we define the angle $\theta_B \equiv \arctan \beta$, with dimensionless ratio $\beta \equiv \delta\omega_B/\Delta_1$. With increasing θ_B the state acquires both a spin and an orbital angular momentum component along $\hat{\mathbf{x}}$. The three-photon transition can now be driven with collinear laser beams, e.g. using $\hat{\mathbf{x}} - \hat{\mathbf{x}} - \hat{\mathbf{z}}$ polarizations [see Fig. 2(b)].

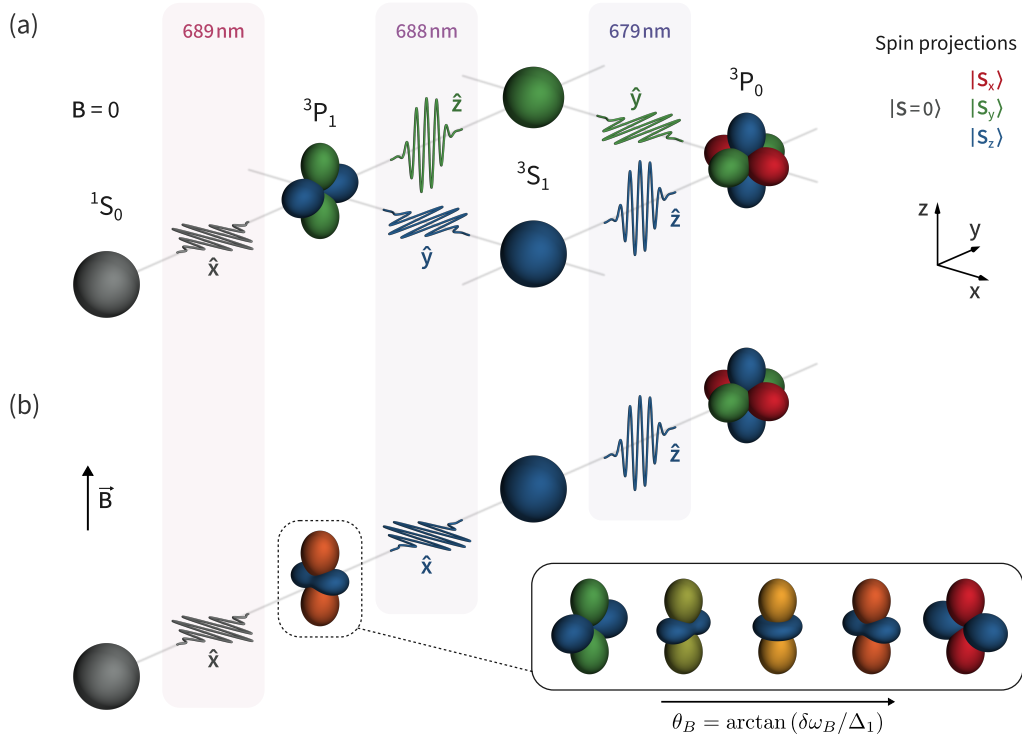


FIG. 2. Engineering a collinear three-photon transition. Cartesian basis representation of the orbital angular momentum (shape) and spin (color) of the atomic wavefunction during the three-photon transition $^1S_0 \rightarrow ^3P_1 \rightarrow ^3S_1 \rightarrow ^3P_0$. While we depict the three-photon process as a sequence of interactions, the coherent excitation is non-sequential and all fields are applied simultaneously. The light fields linking the states are shown with the required polarizations, and spin-preserving transitions (688 nm and 679 nm) are colored according to the spin state $|S_x\rangle$ (red), $|S_y\rangle$ (green), and $|S_z\rangle$ (blue). (a) Contrary to the dipole-allowed transitions, the light at 689 nm causes an excitation orthogonal to its polarization along \hat{x} and changes the spin state. The other two transitions are spin (color) preserving and the light polarizations need to be aligned with the respective p orbitals. To reach the appropriate spin projection of 3P_0 via either $\hat{x}-\hat{y}-\hat{z}$ (blue) or $\hat{x}-\hat{z}-\hat{y}$ (green), at least one of the polarization vectors must have a non-coplanar component with respect to the other two. (b) Applying a magnetic field along \hat{z} deforms the effective angular wavefunction of 3P_1 and permits driving the three-photon transition with collinear light via $\hat{x}-\hat{x}-\hat{z}$ (blue). The inset shows the effective wavefunction for various angles θ_B from 0 to 90 degrees (maximal projection). Note that the collinear combination $\hat{x}-\hat{z}-\hat{x}$ (red) would now also be permitted (not shown).

We demonstrate this coherent three-photon excitation using a thermal ensemble of bosonic ^{88}Sr atoms. In a constant magnetic field aligned with \hat{z} , a single laser pulse containing all three wavelengths is applied to the atoms along the \hat{y} direction. The laser light at 689 and 688 nm is linearly polarized along \hat{x} while the 679 nm component is linearly polarized along \hat{z} . To avoid populating any of the intermediate states, the lasers are each detuned from their respective single-photon resonance by several hundred natural linewidths using an optical frequency comb as a reference. To estimate the three-photon pulse fidelity, we measure the populations in the ground state 1S_0 and in all metastable excited states 3P_J using a state-selective imaging scheme (see Methods).

The resonance frequency for the three-photon transition is given by the effective detuning $\Delta_{\text{eff}} \equiv \Delta_3 + \Omega_{\text{ac}}$, with cumulative laser detuning Δ_3 and ac-Stark shift (see Supplemental):

$$\Omega_{\text{ac}} = -\frac{\Omega_1^2}{2} \frac{\Delta_1}{\Delta_1^2 - \delta\omega_B^2} + \frac{\Omega_3^2}{4\Delta_2}. \quad (5)$$

We vary the laser detuning Δ_3 around the calculated resonance frequency and find the three-photon transition as expected.

Figure 3(a) shows such a line scan with peak excited state transfer of 39% and a line shape that fits to a Voigt profile with HWHM of 59 kHz. This linewidth includes substantial inhomogeneous broadening of 33 kHz, primarily from the thermal Doppler width of the atoms. At the measured three-photon resonance, we scan the pulse duration and observe Rabi oscillations in the 3P_0 population with a frequency of 29.9(2) kHz [see Fig. 3(b)]. This is in good agreement with the expected three-photon Rabi frequency of 30(1) kHz, using a total laser intensity of 4.1 W/cm² and a magnetic field amplitude of 10.1 G (see Methods). The noticeable damping of the Rabi oscillation stems mostly from intensity inhomogeneity across the cloud since we intentionally focus the laser beam to increase the peak intensity. This is easily avoided using a larger beam size. The populations in the other metastable excited states 3P_1 and 3P_2 are small, consistent with minimal off-resonant single-photon excitation.

We further characterize the three-photon process at various magnetic fields and laser detunings by measuring the resonant Rabi frequencies and comparing their magnitudes. It is convenient to parameterize the coupling via the ratio of the

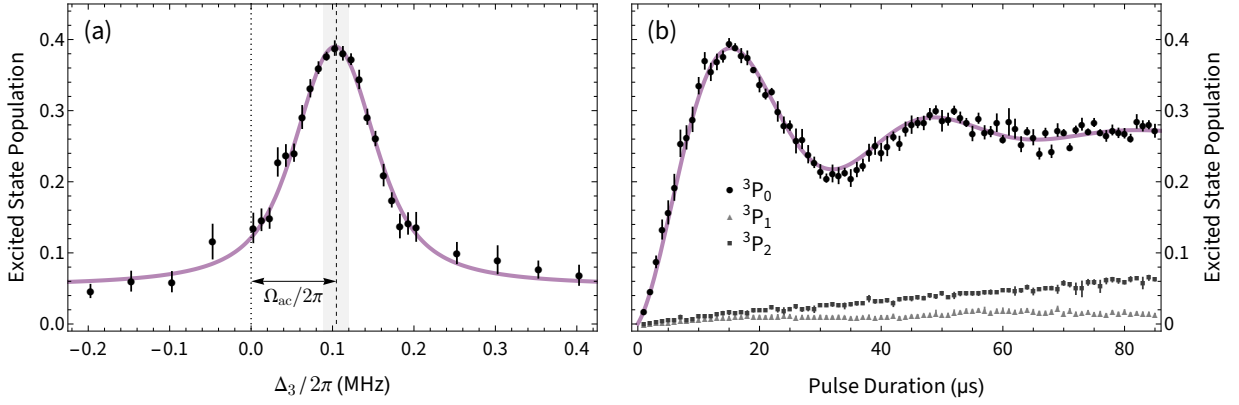


FIG. 3. Coherent three-photon excitation of the $^1S_0 - ^3P_0$ clock transition. (a) Line scan of the three-photon transition showing the fractional excited state population versus the cumulative laser detuning Δ_3 , using $\Delta_1/2\pi = 9.95(1)$ MHz, $\Delta_2/2\pi = -2.54$ GHz, and $\delta\omega_B/2\pi = 21.13(1)$ MHz. Each data point is an average of five measurements and the error bars represent the standard error of the mean. The dashed line and shaded region indicate the expected resonance location and its uncertainty, with a calculated ac-Stark shift of $\Omega_{ac}/2\pi = -105(16)$ kHz. We fit a Voigt profile to the data (solid line) and extract a center frequency of 103.3(9) kHz. (b) Rabi oscillation at the measured three-photon resonance frequency, showing the fractional excited state populations versus the pulse duration. Circles, triangles, and squares indicate the population in the states 3P_0 , 3P_1 , and 3P_2 , respectively. Each data point is an average of five measurements and the error bars represent the standard error of the mean. The fit (solid curve) is an exponentially damped sinusoid with a frequency of 29.9(2) kHz.

detunings $\beta = \delta\omega_B/\Delta_1$ such that Eq. (3) can be written as

$$\Omega_{\text{eff}} = \Omega_0 \frac{\beta}{1 - \beta^2}, \quad (6)$$

where $\Omega_0 \equiv \Omega_1\Omega_2\Omega_3/(2\Delta_1\Delta_2)$ is the maximum Rabi coupling in Eq. (2). In Figure 4(a), we show the normalized three-photon coupling $\Omega_{\text{eff}}/\Omega_0$ over a wide range of detuning ratios β . We find excellent agreement with the expected coupling strength for the effective two-level system based on the inferred single-photon couplings (see Methods). For ratios close to $\beta = 1$, direct excitation to 3P_1 is no longer negligible and the observed Rabi frequencies are slightly lower than predicted. While the strong coupling near this divergence is desirable, sufficient detuning from the single-photon resonance is required to maintain efficient three-photon excitation. We achieve Rabi frequencies as high as 50 kHz while maintaining a detuning of over 500 natural linewidths.

We expect the three-photon coupling to depend on the shape of the effective orbital $|^3P_1, \theta_B\rangle$ and the projection of the light onto it [see Fig. 2(b)]. We define the maximum Rabi coupling at a given magnetic field $\Omega_B \equiv \Omega_0 \sqrt{1 + \beta^2}/(1 - \beta^2)$, such that the three-photon coupling becomes

$$\Omega_{\text{eff}} = \Omega_B \sin \theta_B, \quad \text{for } -\frac{\pi}{2} \leq \theta_B \leq \frac{\pi}{2}. \quad (7)$$

In Figure 4(b), we plot the previous data set in the alternative parametrization $\Omega_{\text{eff}}/\Omega_B$ versus the projection angle θ_B . This normalization avoids the divergence at $\beta = 1$ and shows the sinusoidal variation of the projection, which asymptotes to 1 for large values of β .

At a given Ω_B , the coupling depends on the projection of the atom's dipole moment onto the light polarization vector. Tuning θ_B has the same effect on the coupling as using a polarization for the second light field $\mathbf{e}^{(2)}$ that is impossible to attain with collinear light. For a general elliptical

polarization $\mathbf{e}^{(2)} = \sin \theta \hat{\mathbf{x}} + i \cos \theta \hat{\mathbf{y}}$ with ellipticity angle θ in the xy -plane, the three-photon coupling becomes $\Omega_{\text{eff}} = \Omega_B \cos(\theta_B - \theta)$. In this work we use $\theta = \pi/2$, which is the only polarization choice compatible with collinear propagation along $\hat{\mathbf{y}}$. Thus, the external torque from the magnetic field tunes the effective dipole moment of the atom in much the same way as a waveplate rotates the polarization of light (see Supplemental).

Next, we demonstrate a proof-of-principle clock atom interferometer using the collinear three-photon transition [Fig. 5]. We apply a symmetric Mach-Zehnder pulse sequence [39] consisting of a beamsplitter pulse ($\pi/2$), followed by a mirror pulse (π), and a recombination pulse ($\pi/2$). These pulses are separated by an interrogation time $T = 200 \mu\text{s}$ chosen to be much longer than the lifetimes of the intermediate states. The visibility of the interferometer signal does not vary with the interrogation time, confirming coherent three-photon excitation of the long-lived clock state.

This is the first demonstration of a $^1S_0 - ^3P_0$ clock atom interferometer in ^{88}Sr without the use of a large magnetic bias field [35]. Compared to previous work, we observe a 30-fold increase in Rabi frequency using only 17% of the total laser intensity and 3% of the magnetic field strength [40]. Because of the low magnetic field requirement, our method is applicable in long-baseline atom interferometers, where efficient atom-light interaction is desired anywhere along the baseline [41, 42]. Additionally, the small magnetic field amplitude sets a 3P_0 lifetime of over 10^6 s, significantly longer than the natural lifetime of 118 s in ^{87}Sr [43]. Long coherence times are essential for probing gravity [44] and detecting gravitational waves with long baselines [30, 37]. We also observe more than ten times the Rabi frequency than what could be achieved on the naturally occurring ^{87}Sr clock transition with the same total intensity. High Rabi frequencies ensure broad velocity acceptance [45] and allow for more

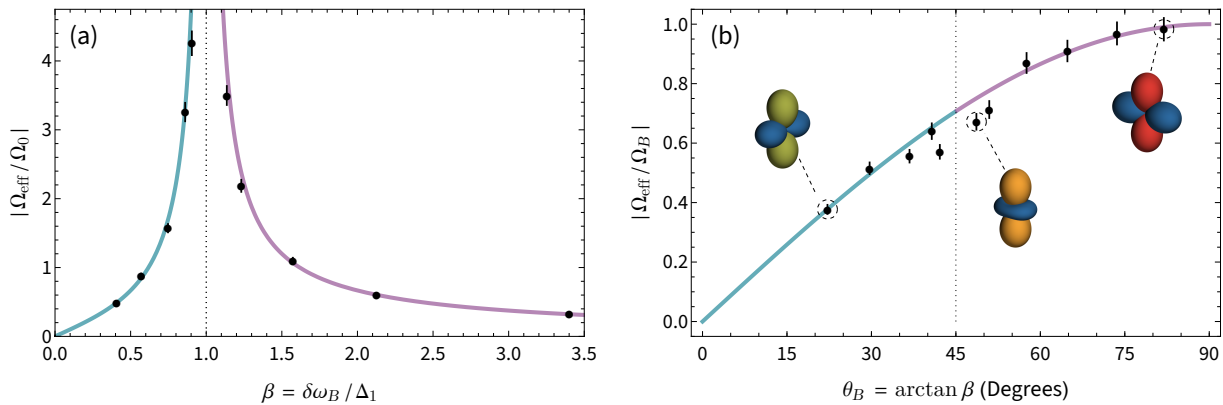


FIG. 4. Dimensionless three-photon coupling and projection angle. (a) Measured normalized Rabi frequencies $|\Omega_{\text{eff}}/\Omega_0|$ as a function of β , where Ω_0 is the predicted maximum coupling strength at $\beta = 0$. Error bars indicate one standard deviation of the combined uncertainty in the measurement of Ω_{eff} and the theoretical prediction of Ω_0 . The solid curves correspond to the expected scaling from Eq. (6). The parameter space is divided into two distinct regions, $\beta < 1$ (teal) and $\beta > 1$ (purple). The coupling strength diverges at $\beta = 1$ (dotted line), which corresponds to the single-photon resonance to the $|^3P_1, m = +1\rangle$ state. For this data, the laser detuning Δ_1 is always positive, but an identical divergence around the $m = -1$ state can be found for negative detunings. (b) The same data in a different normalization $|\Omega_{\text{eff}}/\Omega_B|$, where Ω_B is the maximum coupling at a given magnetic field, versus the projection angle θ_B . The solid curve corresponds to the sinusoid in Eq. (7), with the same colored regions as in (a). Since there is no divergence in this parametrization, the slight deviation from the model around $\theta_B = 45^\circ$ (dotted line) is more apparent. The callouts show the shape of the effective wavefunction $|^3P_1, \theta_B\rangle$ for a selection of data points.

pulses in a given free-fall time, which is beneficial for large momentum transfer (LMT) atom interferometers [42, 46].

Next-generation long-baseline clock atom interferometer experiments, including MAGIS-100 [36] and AION [47], rely on LMT atom optics to significantly enhance their sensitivity. For these applications, interferometry pulses with transfer fidelities above 99% are required [45, 48]. Density matrix simulations suggest that our method can support such pulse efficiencies with W/mm²-scale laser intensities and magnetic fields below 10 G, yielding Rabi frequencies of at least 25 kHz (see Supplemental). Moreover, collinear three-photon transitions enable the use of bosonic isotopes that feature higher natural abundance, simpler level structure, and reduced magnetic field sensitivity. All of these attributes are favorable for reaching the challenging sensitivity targets for gravitational wave detection and dark matter searches with clock atom interferometers.

Driving the $^1S_0 - ^3P_0$ clock transition in bosonic atoms also has many advantages in optical atomic clocks, including insensitivity to the polarization of trapping light, and lack of a first-order Zeeman shift [5, 17, 49]. Existing ^{88}Sr clocks are limited by shifts from the second order Zeeman effect and from the probe light [50–52]. The method described here employs a magnetic field strength that is substantially smaller per unit Rabi frequency, reducing the Zeeman shift for a given coupling strength. In addition, the overall probe light shift can be eliminated with an appropriate choice of laser detunings (see Supplemental). Thus, the three-photon transition demonstrated here appears promising for improving the accuracy of bosonic clocks.

Many of these advantages are also favorable for applications in quantum information science [53], where the bosonic 3P_0 [26, 28, 54, 55] and 3P_2 [56, 57] states show promise for qubit storage and manipulation by leveraging their long

coherence times and environmental insensitivity. While not demonstrated in this work, a similar three-photon excitation $^1S_0 \rightarrow ^3P_1 \rightarrow ^3S_1 \rightarrow ^3P_2$ can be achieved by substituting 707 nm for 679 nm light [22], which may have advantages over magnetic quadrupole excitation to 3P_2 [58, 59].

The method demonstrated here is broadly applicable in other systems that use ultranarrow singlet-to-triplet transitions, especially when high Rabi coupling is beneficial and bosonic isotopes are preferred. In particular, precision measurements based on the differential interrogation of distant atoms benefit from the application of common, copropagating laser pulses.

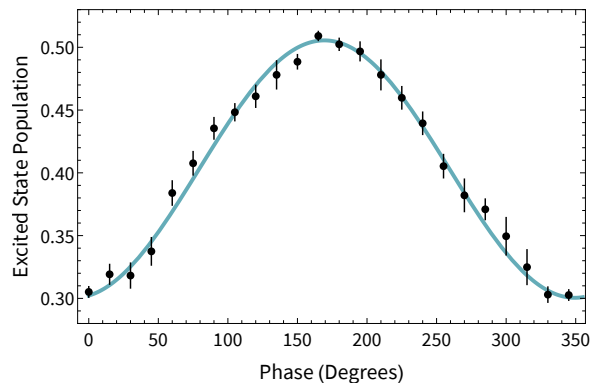


FIG. 5. A three-photon clock atom interferometer with bosonic ^{88}Sr . Normalized 3P_0 excited state population after a Mach-Zehnder pulse sequence versus the laser phase of the first pulse. The pulses are separated by an interrogation time $T = 200 \mu\text{s}$. Every data point is the mean of 10 measurements and error bars indicate the standard error of the mean. The solid line is a sinusoidal fit with a visibility (peak-to-peak amplitude) of 20.5(3)%. The three-photon pulses are applied with $\Delta_1/2\pi = 28.0(1)$ MHz and $\delta\omega_B/2\pi = 21.15(1)$ MHz.

ACKNOWLEDGEMENTS

We wish to thank Mark Kasevich and Shaun Burd for helpful discussions. We thank Leo Hollberg for letting us use his frequency reference. B.G. acknowledges support from the Office of Naval Research through the NDSEG fellowship. This work was supported by the Gordon and Betty Moore Foundation Grant GBMF7945, the NSF QLCI Award No. OMA-2016244, and partially supported by the U.S. Department of Energy, Office of Science, National Quantum Information Science Research Centers, Superconducting Quantum Materials and Systems Center (SQMS) under the contract No. DE-AC02-07CH11359.

Note added. – Upon completion of this manuscript we became aware of related work in ^{84}Sr [60].

APPENDIX: METHODS

Experimental setup

We prepare a thermal ensemble of 10^6 ^{88}Sr atoms at a temperature of 2 μK , using a two-stage magneto-optical trap (MOT). A more detailed description of the setup and experimental sequence for the atomic cloud preparation can be found in Ref. [46]. After the atoms are released from the final MOT, we turn off the magnetic quadrupole field and apply a constant bias field with an amplitude between 4 and 19 G. Then, a three-photon laser pulse of variable duration and detuning is applied to the atoms. The atomic cloud has an rms radius of 130(5) μm at the time of the pulse. The final atomic state is characterized using a state-selective imaging scheme described below.

The three-photon pulses consist of light from three external cavity diode lasers (ECDLs) at 689 nm, 688 nm, and 679 nm. Each ECDL is locked to an optical frequency comb (Menlo Systems FC1500-ULN) that is stabilized to an optical cavity (Menlo Systems 1550 ORS). The relative polarizations of the lasers are set by combining the beams on a polarizing beamsplitter. The combined output is sent through an acousto-optic modulator (AOM) and the diffracted order is coupled into a polarization-maintaining optical fiber. The final three-photon beam at the location of the atoms has a $1/e^2$ radial waist of 392.5(3) μm . The average optical power in each component in the desired polarization is 0.79 mW, 6.9 mW, and 2.2 mW at 689 nm, 688 nm, and 679 nm, respectively. This corresponds to a total peak intensity of 4.1 W/cm^2 .

The 679 nm laser detuning was held fixed for all experiments at -2536 MHz with respect to the $^3\text{P}_0 - ^3\text{S}_1$ resonance, while the 689 nm detuning $\Delta_1/2\pi$ was varied between 4 and 43 MHz. In each case, the 688 nm detuning was adjusted to achieve three-photon resonance ($\Delta_{\text{eff}} = 0$) for the given value of Δ_1 , with a range of -2556 ± 22 MHz with respect to the $^3\text{P}_1 - ^3\text{S}_1$ resonance.

State-selective imaging

To characterize the atomic state after a three-photon pulse, we spatially separate the atoms into three clouds using a sequence of push and repump pulses [see Fig. 6]. Push pulses consist of 461 nm light resonant with the $^1\text{S}_0 - ^3\text{P}_1$ transition, which imparts momentum to atoms in the ground state $^1\text{S}_0$. The first push pulse occurs 200 μs after the end of the three-photon pulse. This time is chosen to give atoms in the $^3\text{P}_1$ state sufficient time to decay to the ground state. To optically pump atoms out of $^3\text{P}_2$, we apply a repump pulse resonant with the $^3\text{P}_2 - ^3\text{S}_1$ transition at 707 nm. Due to the 3:1 branching ratio of this process, most of the atoms return to the ground state, while the rest are shelved in $^3\text{P}_0$. After an additional 200 μs , a second push pulse imparts momentum to the fraction of ground state atoms that were pumped out of $^3\text{P}_2$ and adds additional momentum to the first pushed cloud. Finally, repump light at both 707 nm and 679 nm optically pumps all remaining atoms back into the ground state. We wait 4.5 ms for the three clouds to spatially separate and then count the number of atoms in each cloud using fluorescence imaging on the 461 nm transition. Because of the 3:1 branching ratio, the true $^3\text{P}_2$ population is $4/3$ of the raw atom number in the singly-pushed cloud. Conversely, the true $^3\text{P}_0$ population is obtained by subtracting $1/3$ of the atoms in the singly-pushed cloud from the nominal atom number in the unpushed cloud.

The $^3\text{P}_1$ population is obtained using a modified version of the above imaging sequence [see Fig. 6(b)]. A push pulse immediately following the three-photon pulse separates unexcited ground state atoms from those anywhere in the $^3\text{P}_J$ manifold. After a wait time of 200 μs , a second push pulse imparts momentum to ground state atoms that have decayed

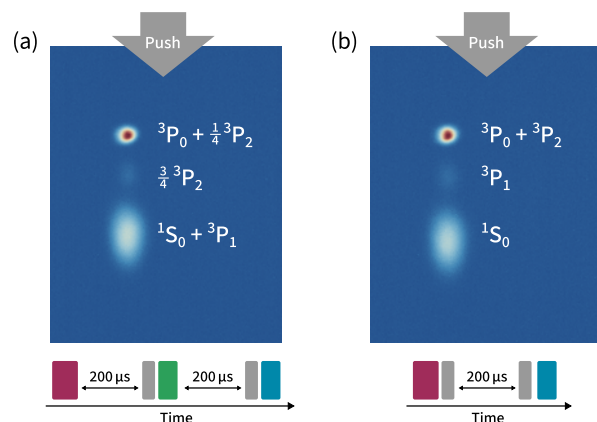


FIG. 6. State-selective imaging schemes. Each scheme produces three spatially separated clouds through the successive application of push pulses, as indicated in the pulse sequences below. Here, red indicates a three-photon pulse, gray a push pulse, while green (707 nm) and blue (679 nm + 707 nm) are repump pulses. (a) The first imaging scheme is designed to determine the $^3\text{P}_0$ and $^3\text{P}_2$ populations, while the $^1\text{S}_0$ and $^3\text{P}_1$ populations cannot be measured independently. (b) The second scheme measures the $^3\text{P}_1$ and $^1\text{S}_0$ populations.

from 3P_1 . Finally, a repump pulse at both 707 nm and 679 nm optically pumps the combined populations of 3P_0 and 3P_2 back into the ground state. The atoms are then imaged after a 4.5 ms wait time as in the other scheme.

Systematic errors

An important caveat to the 3P_1 imaging sequence illustrated in Fig. 6(b) is that it undercounts the loss due to unwanted excitation, since atoms in this state can decay back into the ground state during the three-photon pulse. An estimate for the total loss due to off-resonant scattering from 3P_1 is obtained from the number of scattering events N over the pulse duration t_p , given by

$$N = \frac{1}{\tau_1} \int_0^{t_p} P_e(t) dt \approx \frac{t_p}{\tau_1} \langle P_e \rangle.$$

Here, τ_1 is the lifetime and $P_e(t)$ the state population in 3P_1 , with time averaged fraction $\langle P_e \rangle$. For the data in Fig. 3(b), we estimate $\langle P_e \rangle = 1.2(1)\%$ and $N = 4.8(5)\%$ for the total loss from this channel over the full 85 μ s.

We measure a laser polarization impurity of 2%, which can lead to parasitic excitation to the $|^3P_1, m=0\rangle$ state if the 689 nm detuning is near resonance ($\Delta_1 = 0$). We maintain a detuning of over 500 natural linewidths to avoid competing single-photon processes.

We observe transient magnetic field oscillations when turning on the bias magnetic field. We wait 4.5 ms for the field to settle before applying three-photon pulses. The magnetic field amplitudes B are obtained using Rabi spectroscopy of the 3P_1 Zeeman splitting, which is given by $\delta\omega_B = g_J \mu_B B / \hbar$, where $g_J = 3/2$ is the Landé g factor and μ_B is the Bohr magneton. We measure the Zeeman splittings at the start and 100 μ s after the three-photon pulse and observe a time variation of less than 1%.

Calculating the three-photon coupling

The expected three-photon Rabi frequencies are calculated using Eq. (3) and the three single-photon couplings

$$\Omega_i = \sqrt{\frac{6\pi c^2 \Gamma_i I_i}{\hbar \omega_i^3}}, \quad \text{with } I_i = \frac{P_i}{\frac{\pi}{2} w_0^2}.$$

Here, I_i is the peak intensity of the Gaussian beam with $1/e^2$ radial waist w_0 , and P_i is the optical power in the spherical basis component that connects the specific m states [Fig. 1(b)]. The decay rate for each transition is $\Gamma_i = \eta_i / \tau_i$, where τ_i is the excited state lifetime and η_i is the branching ratio ($\eta_1 = 1$, $\eta_2 = 1/6$, and $\eta_3 = 1/9$). We use the following experimentally determined lifetimes of the intermediate states: 3P_1 ($\tau_1 = 21.28(3)$ μ s) [61] and 3S_1 ($\tau_2 = 15.0(8)$ ns) [62]. To calibrate the laser intensities, we drive resonant Rabi oscillations between $|^1S_0\rangle$ and $|^3P_1, m=0\rangle$ with a measured optical power at 689 nm. The peak Rabi frequency from this measurement serves as an in situ measurement of the effective beam size, with a $1/e^2$ radial waist of 392.5(3) μ m. This effective waist is then approximately common to all three wavelengths, since they are delivered via the same optical fiber and collimation optics. Using the measured powers in each wavelength, we calculate average single-photon Rabi frequencies of approximately $\Omega_1/2\pi = 1.239(1)$ MHz, $\Omega_2/2\pi = 56.0(4)$ MHz, and $\Omega_3/2\pi = 35.8(3)$ MHz.

The detuning of each laser from their respective atomic resonance is inferred using the frequency comb, which we calibrate with the observed 689 nm resonance frequency in conjunction with its best experimental estimate [63]. The uncertainties in Δ_1 and Δ_2 used to calculate Ω_{eff} , Ω_0 , and Ω_B reflect the combined uncertainties from our spectroscopic measurements and the uncertainties in the measured transition frequencies [63, 64]. Our uncertainty in the cumulative laser detuning Δ_3 is lower than the reported uncertainties for the 688 nm and 679 nm transition frequencies. We take advantage of the fact that their difference is equal to the energy splitting between the 3P_1 and 3P_0 states, which is known more precisely [63, 65]. Our uncertainty in the effective three-photon detuning Δ_{eff} reflects the combined uncertainties of the single-photon couplings and detunings.

-
- [1] H. Katori, *Nat. Photon.* **5**, 203 (2011).
 - [2] M. G. Kozlov, M. S. Safronova, J. R. Crespo López-Urrutia, and P. O. Schmidt, *Rev. Mod. Phys.* **90**, 045005 (2018).
 - [3] J. Grotti, S. Koller, S. Vogt, S. Haefner, U. Sterr, C. Lisdat, H. Denker, C. Voigt, L. Timmen, A. Rolland, F. Baynes, H. Margolis, M. Zampaolo, P. Thoumany, M. Pizzocaro, B. Rauf, F. Bregolin, A. Tampellini, P. Barbieri, and D. Calonico, *Nat. Phys.* **14**, 437 (2018).
 - [4] B. J. Bloom, T. L. Nicholson, J. R. Williams, S. L. Campbell, M. Bishof, X. Zhang, W. Zhang, S. L. Bromley, and J. Ye, *Nature* **506**, 71 (2014).
 - [5] A. D. Ludlow, M. M. Boyd, J. Ye, E. Peik, and P. O. Schmidt, *Rev. Mod. Phys.* **87**, 637 (2015).
 - [6] G. E. Marti, R. B. Hutson, A. Goban, S. L. Campbell, N. Poli, and J. Ye, *Phys. Rev. Lett.* **120**, 103201 (2018).
 - [7] S. Blatt, A. D. Ludlow, G. K. Campbell, J. W. Thomsen, T. Zelevinsky, M. M. Boyd, J. Ye, X. Baillard, M. Fouché, R. Le Targat, A. Brusch, P. Lemonde, M. Takamoto, F.-L. Hong, H. Katori, and V. V. Flambaum, *Phys. Rev. Lett.* **100**, 140801 (2008).
 - [8] R. M. Godun, P. B. R. Nisbet-Jones, J. M. Jones, S. A. King, L. A. M. Johnson, H. S. Margolis, K. Szymaniec, S. N. Lea, K. Bongs, and P. Gill, *Phys. Rev. Lett.* **113**, 210801 (2014).
 - [9] M. Takamoto, I. Ushijima, N. Ohmae, T. Yahagi, K. Kokado, H. Shinkai, and H. Katori, *Nat. Photon.* **14**, 411 (2020).

- [10] T. Bothwell, C. J. Kennedy, A. Aeppli, D. Kedar, J. M. Robinson, E. Oelker, A. Staron, and J. Ye, *Nature* **602**, 420 (2022).
- [11] T. Bothwell, D. Kedar, E. Oelker, J. Robinson, S. Bromley, W. Tew, J. Ye, and C. Kennedy, *Metrologia* **56** (2019).
- [12] W. F. McGrew, X. Zhang, R. J. Fasano, S. A. Schäffer, K. Beloy, D. Nicolodi, R. C. Brown, N. Hinkley, G. Milani, M. Schioppo, T. H. Yoon, and A. D. Ludlow, *Nature* **564**, 87 (2018).
- [13] A. P. Kulosa, D. Fim, K. H. Zipfel, S. Rühmann, S. Sauer, N. Jha, K. Gibble, W. Ertmer, E. M. Rasel, M. S. Safronova, U. I. Safronova, and S. G. Porsev, *Phys. Rev. Lett.* **115**, 240801 (2015).
- [14] S. M. Brewer, J.-S. Chen, A. M. Hankin, E. R. Clements, C. W. Chou, D. J. Wineland, D. B. Hume, and D. R. Leibbrandt, *Phys. Rev. Lett.* **123**, 033201 (2019).
- [15] A. V. Taichenachev, V. I. Yudin, C. W. Oates, C. W. Hoyt, Z. W. Barber, and L. Hollberg, *Phys. Rev. Lett.* **96**, 083001 (2006).
- [16] Z. W. Barber, C. W. Hoyt, C. W. Oates, L. Hollberg, A. V. Taichenachev, and V. I. Yudin, *Phys. Rev. Lett.* **96**, 083002 (2006).
- [17] T. Akatsuka, M. Takamoto, and H. Katori, *Nat. Phys.* **4**, 954 (2008).
- [18] R. Santra, E. Arimondo, T. Ido, C. H. Greene, and J. Ye, *Phys. Rev. Lett.* **94**, 173002 (2005).
- [19] T. Hong, C. Cramer, W. Nagourney, and E. N. Fortson, *Phys. Rev. Lett.* **94**, 050801 (2005).
- [20] V. D. Ovsiannikov, V. G. Pal'chikov, A. V. Taichenachev, V. I. Yudin, H. Katori, and M. Takamoto, *Phys. Rev. A* **75**, 020501(R) (2007).
- [21] E. A. Alden, K. R. Moore, and A. E. Leanhardt, *Phys. Rev. A* **90**, 012523 (2014).
- [22] D. S. Barker, N. C. Pistenti, B. J. Reschovsky, and G. K. Campbell, *Phys. Rev. A* **93**, 053417 (2016).
- [23] G. Grynberg, B. Cagnac, and F. Biraben, Multiphoton resonant processes in atoms, in *Coherent Nonlinear Optics: Recent Advances* (Springer, 1980) pp. 111–164.
- [24] G. Panelli, S. C. Burd, E. J. Porter, and M. Kasevich, arXiv (2024), arXiv:2403.09814.
- [25] I. S. Madjarov, J. P. Covey, A. L. Shaw, J. Choi, A. Kale, A. Cooper, H. Pichler, V. Schkolnik, J. R. Williams, and M. Endres, *Nat. Phys.* **16**, 857 (2020).
- [26] N. Schine, A. Young, W. Eckner, M. Martin, and A. Kaufman, *Nat. Phys.* **18** (2022).
- [27] W. Eckner, N. Oppong, A. Cao, A. Young, W. Milner, J. Robinson, J. Ye, and A. Kaufman, *Nature* **621**, 734 (2023).
- [28] A. Cao, W. J. Eckner, T. L. Yelin, A. W. Young, S. Jandura, L. Yan, K. Kim, G. Pupillo, J. Ye, N. D. Oppong, and A. M. Kaufman, arXiv (2024), arXiv:2402.16289.
- [29] N. Hinkley, J. A. Sherman, N. B. Phillips, M. Schioppo, N. D. Lemke, K. Beloy, M. Pizzocaro, C. W. Oates, and A. D. Ludlow, *Science* **341**, 1215 (2013).
- [30] S. Kolkowitz, I. Pikovski, N. Langellier, M. D. Lukin, R. L. Walsworth, and J. Ye, *Phys. Rev. D* **94**, 124043 (2016).
- [31] M. Schioppo, R. Brown, W. McGrew, N. Hinkley, R. Fasano, K. Beloy, T. H. Yoon, G. Milani, D. Nicolodi, J. Sherman, N. Phillips, C. Oates, and A. Ludlow, *Nat. Photon.* **11**, 48 (2016).
- [32] E. Oelker, R. Hutson, C. Kennedy, L. Sonderhouse, T. Bothwell, A. Goban, D. Kedar, C. Sanner, J. Robinson, G. Marti, D. Matei, T. Legero, M. Giunta, R. Holzwarth, F. Riehle, U. Sterr, and J. Ye, *Nature Photon* **13** (2019).
- [33] Boulder Atomic Clock Optical Network (BACON) Collaboration, *Nature* **591**, 564 (2021).
- [34] X. Zheng, J. Dolde, V. Lochab, B. Merriman, H. Li, and S. Kolkowitz, *Nature* **602**, 425 (2022).
- [35] L. Hu, N. Poli, L. Salvi, and G. M. Tino, *Phys. Rev. Lett.* **119**, 263601 (2017).
- [36] M. Abe, P. Adamson, M. Borcean, D. Bortoletto, K. Bridges, S. P. Carman, S. Chattopadhyay, J. Coleman, N. M. Curfman, K. DeRose, *et al.*, *Quantum Sci. Technol.* **6**, 044003 (2021).
- [37] P. W. Graham, J. M. Hogan, M. A. Kasevich, and S. Rajendran, *Phys. Rev. Lett.* **110**, 171102 (2013).
- [38] Though we only show the case where the first photon is \hat{x} -polarized, the requirement for non-coplanar polarizations is independent of the choice of the first polarization for any $\mathbf{e}^{(1)} \perp \mathbf{B}$.
- [39] M. A. Kasevich and S. Chu, *Phys. Rev. Lett.* **67**, 181 (1991).
- [40] L. Hu, E. Wang, L. Salvi, J. N. Tinsley, G. M. Tino, and N. Poli, *Class. Quantum Grav.* **37**, 014001 (2019).
- [41] J. Hartwig, S. Abend, C. Schubert, D. Schlippert, H. Ahlers, K. Posso-Trujillo, N. Gaaloul, W. Ertmer, and E. M. Rasel, *New J. Phys.* **17**, 035011 (2015).
- [42] T. Kovachy, P. Asenbaum, C. Overstreet, C. A. Donnelly, S. M. Dickerson, A. Sugarbaker, J. M. Hogan, and M. A. Kasevich, *Nature* **528**, 530 (2015).
- [43] J. A. Muniz, D. J. Young, J. R. K. Cline, and J. K. Thompson, *Phys. Rev. Res.* **3**, 023152 (2021).
- [44] V. Xu, M. Jaffe, C. D. Panda, S. L. Kristensen, L. W. Clark, and H. Müller, *Science* **366**, 745 (2019).
- [45] T. Wilkason, M. Nantel, J. Rudolph, Y. Jiang, B. E. Garber, H. Swan, S. P. Carman, M. Abe, and J. M. Hogan, *Phys. Rev. Lett.* **129**, 183202 (2022).
- [46] J. Rudolph, T. Wilkason, M. Nantel, H. Swan, C. M. Holland, Y. Jiang, B. E. Garber, S. P. Carman, and J. M. Hogan, *Phys. Rev. Lett.* **124**, 083604 (2020).
- [47] L. Badurina, E. Bentine, D. Blas, K. Bongs, D. Bortoletto, *et al.*, *J. Cosmol. Astropart. Phys.* **2020** (05), 011.
- [48] A. Béguin, T. Rodzinka, L. Calmels, B. Allard, and A. Gauguier, *Phys. Rev. Lett.* **131**, 143401 (2023).
- [49] X. Baillard, M. Fouché, R. Targat, P. Westergaard, A. Lecallier, Y. Le Coq, G. Rovera, S. Bize, and P. Lemonde, *Opt. Lett.* **32**, 1812 (2007).
- [50] T. Akatsuka, M. Takamoto, and H. Katori, *Phys. Rev. A* **81**, 023402 (2010).
- [51] S. Origlia, M. S. Pramod, S. Schiller, Y. Singh, K. Bongs, R. Schwarz, A. Al-Masoudi, S. Dörscher, S. Herbers, S. Häfner, U. Sterr, and C. Lisdat, *Phys. Rev. A* **98**, 053443 (2018).
- [52] M. A. Norcia, A. W. Young, W. J. Eckner, E. Oelker, J. Ye, and A. M. Kaufman, *Science* **366**, 93 (2019).
- [53] R. Stock, N. S. Babcock, M. G. Raizen, and B. C. Sanders, *Phys. Rev. A* **78**, 022301 (2008).
- [54] A. Young, W. Eckner, W. Milner, D. Kedar, M. Norcia, E. Oelker, N. Schine, J. Ye, and A. Kaufman, *Nature* **588**, 408 (2020).
- [55] A. Pagano, S. Weber, D. Jaschke, T. Pfau, F. Meinert, S. Montangero, and H. P. Büchler, *Phys. Rev. Res.* **4**, 033019 (2022).
- [56] D. Okuno, Y. Nakamura, T. Kusano, Y. Takasu, N. Takei, H. Konishi, and Y. Takahashi, *J. Phys. Soc. Jpn.* **91**, 084301 (2022).
- [57] J. Trautmann, D. Yankelev, V. Klüsener, A. J. Park, I. Bloch, and S. Blatt, *Phys. Rev. Res.* **5**, 013219 (2023).
- [58] S. Pucher, V. Klüsener, F. Spriestersbach, J. Geiger, A. Schindewolf, I. Bloch, and S. Blatt, *Phys. Rev. Lett.* **132**, 150605 (2024).
- [59] V. Klüsener, S. Pucher, D. Yankelev, J. Trautmann, F. Spriestersbach, D. Filin, S. G. Porsev, M. S. Safronova, I. Bloch, and S. Blatt, *Phys. Rev. Lett.* **132**, 253201 (2024).
- [60] J. He, B. Pasquiou, R. G. Escudero, S. Zhou, M. Borkowski, and F. Schreck, Coherent three-photon excitation of the strontium clock transition (2024), arXiv:2406.07530.

- [61] T. L. Nicholson, S. L. Campbell, R. B. Hutson, G. E. Marti, B. J. Bloom, R. L. McNally, W. Zhang, M. D. Barrett, M. S. Safronova, G. F. Strouse, W. L. Tew, and J. Ye, *Nat. Commun.* **6**, 6896 (2015).
- [62] G. Jönsson, C. Levinson, A. Persson, and C.-G. Wahlström, *Z. Phys. A - Atoms and Nuclei* **316**, 255 (1984).
- [63] G. Ferrari, P. Cancio, R. Drullinger, G. Giusfredi, N. Poli, M. Prevedelli, C. Toninelli, and G. M. Tino, *Phys. Rev. Lett.* **91**, 243002 (2003).
- [64] I. Courtillot, A. Quessada-Vial, A. Brusch, D. Kolker, G. Rovera, and P. Lemonde, *Eur. Phys. J. D.* **33**, 161 (2005).
- [65] P. Morzyński, M. Bober, D. Bartoszek-Bober, J. Nawrocki, P. Krehlik, L. Śliwczyński, M. Lipinski, P. Masłowski, A. Cygan, P. Dunst, M. Garus, D. Lisak, J. Zachorowski, G. Wojciech, C. Radzewicz, R. Ciuryło, and M. Zawada, *Sci. Rep.* **5**, 17495 (2015).